

Fundamental Materialistic Properties of ZnSnP₂ for Solar Energy Conversion and Environmental Friendly Photovoltaic Devices

NEERAJ¹, PRAVESH², SURESH PAL³, SARITA KUMARI⁴, A. S. VERMA^{1,*}

¹Department of Physics, Banasthali Vidyapith, Rajasthan, 304022, INDIA

²Department of Electronics and communication, KIET Group of Institutions, Ghaziabad, Uttar Pradesh, 201206, INDIA

³Department of Applied Science, World College of Technology and Management, Haryana, 122506 INDIA,

⁴Department of Physics, University of Rajasthan, Jaipur, (India) 302004

Abstract: - Ab initio calculations have been performed by the full potential linearized augmented plane wave (FP-LAPW) method as implemented in the WIEN2K code within the density functional theory to obtain the fundamental physical properties of ZnSnP₂ in the body centered tetragonal (BCT) phase. The six elastic constants (C_{11} , C_{12} , C_{13} , C_{33} , C_{44} and C_{66}) and mechanical parameters have been presented and compared with the available experimental data. The thermal properties within the quasi-harmonic approximation is used to give an accurate description of the pressure-temperature dependence of the thermal-expansion coefficient, bulk modulus, specific heat, Debye temperature, entropy Grüneisen parameters. Based on the semi-empirical relation, we have determined the hardness of the material; which attributed to different covalent bonding strengths. Further, ZnSnP₂ solar cell devices have been modeled; device physics and performance parameters have analyzed for ZnTe and CdS buffer layers. Simulation results for ZnSnP₂ thin layer solar cell show the maximum efficiency (22.9%) with ZnTe as the buffer layer. Most of the investigated parameters are reported for the first time.

Key-Words: - Electronic properties, Elastic constants, Thermodynamic properties, Photovoltaic device.

Received: December 8, 2019. Revised: February 21, 2020. Accepted March 21, 2020. Published: March 27, 2020.

1 Introduction

ZnSnP₂ is a member of A^{II}B^{IV}C₂^V group ternary compound semiconductors, which has with chalcopyrite structure as a new solar absorber. The growth of ZnSnP₂ thin films has been prepared by co-evaporation and in ultra high vacuum by molecular beam epitaxy (MBE). Recently [1], ZnSnP₂ based thin-film solar cell is fabricated and also prepared energy band gap by phosphidation method under the variation of Zn/Sn atomic ratio. Defects introduce localized levels in the energy gap of ZnSnP₂ and other compound semiconductors through which they control solar cell device performance, efficiency and reliability.

In ZnSnP₂ thin film, zinc vacancies or zinc-on-tin sites are considered as acceptor. This is responsible for p-type conductivity. ZnSnP₂ is focused as a solar absorbing material consisting of safe and earth-abundant elements. Investigated the structures of

interfaces related to the absorbing material ZnSnP₂ to clarify the origin of high resistance and improve the photovoltaic performance in ZnSnP₂ solar cells. The absorption coefficient of ZnSnP₂ was reported to be approximately 10^5 cm^{-1} in visible light range; ZnSnP₂ has a promising property for a solar absorbing material. ZnSnP₂ crystals for solar cells were prepared by mechanical-polishing [2,3].

Martinez et al [4], the A^{II}B^{IV}C₂^V materials have similarly compelling electronic properties to their A^{II}B^V counter parts. Materials can typically be doped both n-type and p-type using extrinsic impurities, and mobilities can be extremely high, with multiple reports. The phosphide and arsenide in A^{II}B^{IV}C₂^V compounds have been synthesized in bulk form by three primary techniques; while optical properties have been studied using a combination of theory and experiment. Experimental work has been used to examine photoluminescence and absorption edge, while

calculations can provide insight into physical mechanisms underlying these measurements [4].

This material has been proposed as a promising candidate for a solar absorbing material and $\text{Cu}_2\text{ZnSnS}_{4-x}\text{Se}_x$, Cu_2SnS_3 , Cu_2O , SnS , Fe_2S , and Zn_3P_2 solar cells have been developed with a conversion efficiency of 12.6% [5]. ZnSnP_2 has a direct band gap of 1.6 eV [6].

Ternary $\text{A}^{\text{II}}\text{B}^{\text{IV}}\text{C}_2^{\text{V}}$ chalcopyrite semiconductors (Zn,Cd)(Si,Ge,Sn)(P,As)₂ have band gap energies ranging from 2.1 eV (ZnSiP_2) to 0.67 eV (ZnSnAs_2) [6]. These materials have structural as well as electronic anomaly with higher energy gaps and lower melting points relative to their binary analogues, because of which they are considered to be important in crystal growth studies and device applications. Apart from it, the other important technological applications of these materials are in light emitting diodes, infrared detectors, infrared oscillations, etc [4-8]. ZnSnP_2 semiconductors open up the possibility of fabricating a graded multi-junction solar cell using the ordered chalcopyrite as the top layer, with progressively more disordered layers underneath, free from lattice matching problems [7-10]. In spite of all these work, it has been seen that the theoretical results obtained for elastic constants which experimentally need single crystals of these compounds differ considerably with the available experimental data [4-8]. A considerable amount of experimental and theoretical work related to the prediction of crystal structures, lattice constants, phase diagrams and related properties of these compounds has been done during the last few years [9-13].

In the present article, we have been investigated the structural, electronic, optical, elastic and thermal properties of ZnSnP_2 in chalcopyrite phase. We have presented the theoretical study of expansion coefficient (α), heat capacities (C_v and C_p), bulk modulus (B and B'), Debye temperature (θ_D), hardness (H) and Gruneisen parameter (γ) of ZnSnP_2 ; which are nevertheless scarce in literature. Calculated ground-state structural properties of the aforementioned crystals have been compared with available experimental and theoretical data. The outline of the paper is as follows. In section II we have given a brief review of the computational scheme used. The calculations of the fundamental physical properties have been described with the application point of view in solar cell device in section III; while the summary and conclusions are drawn in section VI.

2 Problem Formulation

The calculations were done using FP-LAPW computational scheme [14, 15] as implemented in the WIEN2K code [16]. The FP-LAPW method expands the Kohn-Sham orbitals as atomic like orbitals inside the muffin-tin (MT) atomic spheres and plane waves in the interstitial region. The Kohn-Sham equations were solved using the recently developed Wu-Cohen generalized gradient approximation (WC-GGA) [17, 18] for the exchange-correlation (XC) potential. It has been shown that this new functional is more accurate for solids than any existing GGA and meta-GGA forms. For a variety of materials, it improves the equilibrium lattice constants and bulk moduli significantly over local-density approximation [19] and Perdew-Burke-Ernzerhof (PBE) [20] and therefore is a better choice. For this reason we adopted the new WC approximation for the XC potential in studying the present systems. Further for electronic structure calculations modified Becke-Johnson potential (mBJ) [21] as coupled with WC-GGA is used.

The valence wave functions inside the atomic spheres were expanded up to $l=10$ partial waves. In the interstitial region, a plane wave expansion with $R_{\text{MT}}K_{\text{max}}$ equal to seven was used for all the investigated systems, where R_{MT} is the minimum radius of the muffin-tin spheres and K_{max} gives the magnitude of the largest K vector in the plane wave expansion. The potential and the charge density were Fourier expanded up to $G_{\text{max}} = 10$. We carried out convergence tests for the charge-density Fourier expansion using higher G_{max} values. The R_{MT} (muffin-tin radii) are taken to be 2.2, 2.22 and 1.7 (in atomic unit) for Zn, Ge and P respectively. The modified tetrahedron method [22] was applied to integrate inside the Brillouin zone (BZ) with a dense mesh of 5000 uniformly distributed k -points (equivalent to 405 in irreducible BZ) where the total energy converges to less than 10^{-6} Ry.

The computer simulation tool AMPS-1D (Analysis of Microelectronic and Photonic Structures) was employed by specifying semiconductor parameters as input in each layers of the cell.

3 Problem Solution

3.1 Structural, electronic and optical Properties

The ternary chalcopyrite semiconductor crystallizes in the chalcopyrite structure with space group $I-42d$ (D_{2d}^{12}). The Zn atom is located at (0,0,0); (0,1/2,1/4), Ge at (1/2,1/2,0); (1/2,0,1/4) and P at (u,1/4,1/8); (-u,3/4,1/8); (3/4,u,7/8); (1/4,-u,7/8). Two unequal bond lengths d_{Zn-P} and d_{Ge-P} result in two structural deformations, first is characterized by u parameter defined as $u=0.25 + (d_{Zn-P} - d_{Ge-P})/a^2$ where a is the lattice parameter in x and y direction, and the second parameter $\eta=c/a$, where c is lattice parameter in z direction which is generally different from 2a.

To determine the best energy as a function of volume, we minimized the total energy of the system with respect to the other geometrical parameters. The final optimal curve of total energy is obtained by minimizing the energy verses [V, c/a (V), u (V)] by FP-LAPW calculations and Murnaghan equation of state [23]. Table 1 present the lattice parameters (a, c and u) and obtained along with the bulk modulus (B) and its pressure derivative (B'). The calculated total energy per unit as a function of volume is shown in Figure 1. The present calculations using the WC-mBJ method yields a pseudo-direct band gap of 2.0 eV as shown in figure 2. As clear from the figures 1 (b) that the obtained electronic band gap matches well with the experimental data predicted by Shaposhnikov et al [24]. Scanlon et al, [8] and Sahin et al [12] reported an estimate of the theoretical band gap of ZnGeP₂ as 1.73 eV. The mBJ potential gives results in good agreement with experimental values that are similar to those produced by more sophisticated methods but at much lower computational costs [21].

The imaginary part $\epsilon_2(\omega)$ of the dielectric function could be obtained from the momentum matrix elements between the occupied and unoccupied wave functions and real part $\epsilon_1(\omega)$ can be evaluated using the Kramer-Kronig relations [25-28]. Figure 3 (a) and (b) displays the real and imaginary parts respectively of the electronic dielectric function $\epsilon(\omega)$ spectrum. The main peaks of $\epsilon_1(\omega)$, occurs at 2.73 eV (17.14) and $\epsilon_1(\omega)$ spectra further decreases up to 7.31 eV. Optical spectra exhibit anisotropy in two directions (along basal-plane and z-axis) with a very small difference (0.2034 eV) in the static limit. Figure 3 (b) displays the imaginary (absorptive) part

of the dielectric function $\epsilon_2(\omega)$ and shows that the critical points of the $\epsilon_2(\omega)$ occurs at 2.0 eV. The obtained fundamental edges are closely related to the obtained energy band gap values 2.0 eV.

The obtained values of band gap, refractive index and dielectric constant are presented in table 2 and compared with the available reported data. Figure 4 presents the refractive index $n(\omega)$ along with the extinction coefficient $k(\omega)$. The refractive index spectrum shows an anisotropic behavior ($\Delta n(0 \text{ eV})=0.0334$), hence only the average is listed in (3.04375) table 2. The peak value of refractive indices is 4.18 at 2.73 eV.

Figure 4 also show extinction coefficient $k(\omega)$ is related to the decay or damping of the oscillation amplitude of the incident electric field, the extinction coefficient $k(\omega)$ decreases with increasing the incident photon energy.

The calculated optical reflectivity $R(\omega)$ is displayed in Figure 5 (a) and this has small reflectivity in the low energy range. The maximum reflectivity occurs in region 4.22-14.67 eV [30].

The absorption coefficient is a parameter, which indicates the fraction of light lost by the electromagnetic wave, when it passes through a unit thickness of the material. These have been plotted in figure 5 (b). It is clear that polarization has a minor influence on the spectrum. From the absorption spectrum, we can easily find the absorption edges located at 1.99 eV. It is clear from the above discussion that both chalcopyrites are excellent mid-IR transparent crystal materials as they transparent to low energy photons showing zero value of the absorption coefficient in that region. When the photon energy is more than the absorption edge value, then adsorption coefficient increases. The absorption coefficients further decrease rapidly in the high energy region, which is the typical characteristic of semiconductors. Optical conductivity parameters are closely related to the photo-electric conversion efficiency and mainly used to measure the change caused by the illumination. Figure 5 (c) shows the optical conductivity and it's clear that the maximum photoconductivity of the materials lies in the u-v region of electromagnetic spectrum.

3.2 Elastic Properties

The deformations [31] are shown in Table 3 and chosen such that the strained systems have the maximum possible symmetry. The elastic stiffness tensor of chalcopyrite compounds has six independent components because of the symmetry

properties of the D_{2d}^{12} space group, namely C_{11} , C_{12} , C_{13} , C_{33} , C_{44} and C_{66} in Young notation. The calculated elastic constant for the tetragonal phase of $ZnGeP_2$ are listed in Table 4.

Voigt and Reuss approximations provides [32-35], in fact, an estimation of the elastic behaviour of an isotropic material, for instance a polycrystalline sample. We have found bulk (B in GPa) and shear modulus (G in GPa). Pugh [36] proposed that the resistance to plastic deformation is related to the product Gb , where 'b' is the Burgers vector, and that the fracture strength is proportional to the product Ba , where 'a' corresponds to the lattice parameter. As b and a are constants for specific materials, the Ba/Gb can be simplified into B/G . This formula was recently exploited in the study of brittle vs ductile transition in intermetallic compounds from first-principles calculations [37, 38]. A high B/G ratio is associated with ductility, whereas a low value corresponds to the brittle nature. The critical value which separates ductile and brittle material is around 1.75, i.e., if $B/G > 1.75$, the material behaves in a ductile manner otherwise the material behaves in a brittle manner. We have found that B/G ratios are 1.78 and classifying the materials is ductile.

3.3 Thermal Properties

To investigate the thermodynamic properties of Zn-chalcopyrite, we have used Gibbs program. The obtained set of total energy versus primitive cell volume determined in previous section has been used to derive the macroscopic properties as a function of temperature and pressure from the standard thermodynamic relations. Gibbs program is based on the quasi-harmonic Debye model [39], in which the non-equilibrium Gibbs function $G^*(V; P, T)$ can be written in the form of:

$$G^*(V; P, T) = E(V) + PV + A_{vib}[\theta_D; T] \quad (1)$$

where $E(V)$ is the total energy per unit cell, PV corresponds to the constant hydrostatic pressure condition, θ_D is the Debye temperature, and A_{vib} is the vibrational term, which can be written using the Debye model of the phonon density of states as [40, 41]:

$$A_{vib}[\theta_D; T] = nkT \left[\frac{9\theta}{8T} + 3 \ln(1 - e^{-\theta/T}) - D\left(\frac{\theta}{T}\right) \right] \quad (2)$$

where n is the number of atoms per formula unit, $D(\theta/T)$ represents the Debye integral, and for an isotropic solid, θ is expressed as [40]:

$$\theta_D = \frac{\hbar}{k} \left[6\pi^2 V^{1/2} n \right]^{1/3} f(\sigma) \sqrt{\frac{B_s}{M}} \quad (3)$$

M being the molecular mass per unit cell and B_s the adiabatic bulk modulus, approximated by the static compressibility [39]:

$$B_s \cong B(V) = V \frac{d^2 E(V)}{dV^2} \quad (4)$$

$f(\sigma)$ is given by Refs. [39, 42, 43]; where σ is the Poisson ratio.

Therefore, the non-equilibrium Gibbs function $G^*(V; P, T)$ as a function of $(V; P, T)$ can be minimized with respect to volume V ,

$$\left(\frac{\partial G^*(V; P, T)}{\partial V} \right)_{P, T} = 0 \quad (5)$$

By solving Eq. (17), one can obtain the thermal equation of state (EOS) $V(P, T)$. The heat capacity C_V and the thermal expansion coefficient α are given by [35],

$$C_V = 3nk \left[4D\left(\frac{\theta}{T}\right) - \frac{3\theta/T}{e^{\theta/T} - 1} \right] \quad (6)$$

$$S = nk \left[4D\left(\frac{\theta}{T}\right) - 3 \ln(1 - e^{-\theta/T}) \right] \quad (7)$$

$$\alpha = \frac{\gamma C_V}{B_T V} \quad (8)$$

where γ is the Grüneisen parameter, which is defined as:

$$\gamma = - \frac{d \ln \theta(V)}{d \ln V} \quad (9)$$

Through the quasi-harmonic Debye model, one could calculate the thermodynamic quantities of any temperatures and pressures of compounds from the calculated $E-V$ data at $T = 0$ and $P = 0$. We can also provide a prediction of the hardness (H in GPa) by using the semi-empirical equations developed by Verma and co-authors [44],

$$H = K B^{K+1} \quad (10)$$

$B =$ Bulk modulus; $K = 0.59$ for $A^{II}B^{IV}C_2^V$

To determine the thermodynamic properties through the quasi-harmonic Debye model, a temperature range 0 K-1000 K has been taken. The pressure effects are studied in the 0–8 GPa range. Figure 6 (a) presents relationships between the equilibrium volume V (bohr³) and pressure at various temperatures. Meanwhile, V increases slightly as the temperature increases, whereas the equilibrium volume V decreases dramatically as the pressure P increases at a given temperature. This account suggests that the ZnGeP₂ under loads turns to be more compressible with increasing pressure than decreases temperature. Furthermore, It is noted that the relationship between the bulk modulus and temperature in Figure 6 (b). The bulk modulus slightly decreases with increasing temperature at a given pressure and increases with increasing pressure at a given temperature. The variation of the Debye temperature θ_D (K) as a function of pressure and temperature illustrated by proposed results is displayed in Figure 6 (d).

With the applied pressure increasing, the Debye temperatures are almost linearly increasing. Figure 6 (e) shows the volume thermal expansion coefficient α (10⁻⁵/K) at various pressures, from which it can be seen that the volume thermal expansion coefficient α increases quickly at a given temperature particularly at zero pressure below the temperature of 300 K.

After a sharp increase, the volume thermal expansion coefficient is nearly insensitive to the temperature above 300 K due to the electronic contributions. As very important parameters, the heat capacities of a substance not only provide essential insight into the vibrational properties but are also mandatory for many applications.

The proposed calculation of the heat capacities C_p and C_v verses temperature at pressure range 0-8 GPa are shown in the following Figure 7. From these figures, we can see that the constant volume heat capacity C_v and the constant pressure capacity C_p are very similar in appearance and both of them are proportional to T^3 at low temperatures. At high temperatures, the anharmonic effect on heat capacity is suppressed; which is called Dulong-Petit limit, with the increasing of the temperature, whereas C_p increases monotonically with the temperature.

Figure 8 (a) shows the entropy vs temperature at various pressures. The entropies are variable by power exponent with increasing temperature but the entropies are higher at low pressure than that at high pressure at same temperature. In figure 8 (b), we have shown the values of Grüneisen parameter γ at

different temperatures and pressures. It shows the value γ increases as the temperature increases at a given pressure and decreases as the pressure increases at a given temperature.

In figure 8 (c), we have shown the values of hardness (H in GPa) at different temperatures and pressures. It shows the hardness decreases as the temperature increases at a given pressure and increases as the pressure increases at a given temperature. The values of hardness are reported for the first time at different pressure and temperature. Table 1 present the thermal properties such as isothermal bulk modulus, hardness, Grüneisen parameter, Debye temperature and thermal expansion coefficient at 300 K. The Grüneisen parameter γ is another important quantity for the materials.

3.4 Cell structure, material parameters and cell performance

The modeled cell structure is shown in Figure 9 (a). The simulated structure starts with 2500 nm ZnGeP₂ layer over a Molybdenum substrate followed by 50 nm CdS/ZnSe buffer and 50 nm intrinsic ZnO window layer with 300 nm Al doped ZnO layer. The device simulation is based on the solution of a set of equations, which provide a mathematical model for device operation. Using this model, the influence of the modeling parameters over the efficiency of the device can be examined, which is a tedious task by experimental method. The simulation is based on the solution of one dimensional Poisson equation and the continuity equations for free charge carriers. These equations are expressed as follows:

$$\frac{d}{dx} \left(-\varepsilon(x) \frac{d\psi}{dx} \right) = q [p(x) - n(x) + N_D^+(x) - N_A^-(x) + p_t(x) - n_t(x)] \quad (11)$$

$$\frac{dp_p}{dt} = G_p - \frac{p_p - p_{p0}}{\tau_p} - p_p \mu_p \frac{dE}{dx} - \mu_p E \frac{dp_p}{dx} + D_p \frac{d^2 p_p}{dx^2} \quad (12)$$

$$\frac{dn_p}{dt} = G_n - \frac{n_p - n_{p0}}{\tau_n} + n_p \mu_n \frac{dE}{dx} + \mu_n E \frac{dn_p}{dx} + D_n \frac{d^2 n_p}{dx^2} \quad (13)$$

Where ε the permittivity, q the charge, Ψ the electrostatic potential, n the free electron density, p the free hole density, $p_t(x)$ the trapped hole density, $n_t(x)$ the trapped electron density, N_D^+ the donor atom density, N_A^- the acceptor atom density, E the electric field and G the generation rate, D the diffusion coefficient, τ the lifetime and μ the mobility of charge carriers. With the help of solution of these equations current density/voltage

(J/V) characteristics are determined and performance of solar cell with different buffer layers is compared. In Table 5 we have presented description for the parameters; which was used in the simulation. The terrestrial spectrum AM 1.5 (Air Mass 1.5 Global 1000W/m²) is used for illumination. The schematic energy band diagram under equilibrium condition for the thin layer solar cell has been illustrated in Figure 9 (b). The band diagram is drawn according to Anderson's affinity rule, which shows conduction band offset is $\Delta E_c = \chi_2 - \chi_1$ and valance band offset is $\Delta E_v = (\chi_1 + E_{g1}) - (\chi_2 + E_{g2})$. The band diagram shows that this is a type II heterostructure. The difference in band gaps creates discontinuity spikes in the conduction- and valance bands. These spikes can create extra barriers for the electrons to overcome or tunnel through, and may also work as potential wells with discrete energy states [52]. The Figure 9 (c) shows the illuminated characteristics *J-V* curve of the proposed solar cell structures. The performance parameters open circuit voltage (V_{oc}), short circuit current density (J_{sc}), Fill Factor (*FF*) and efficiency (η) have been calculated from *J-V* characteristics for different considered buffer layers. The simulation results have been presented in Table 6 (a) and 6 (b). These results show that both the buffer layers provide good efficiency (>20%). A maximum density of current (>29 mA/cm²) has been obtained with both the buffer layers, which ensures the suitability of CdS and ZnSe buffer layers in ZnGeP₂ solar cells. Further, the analysis of photoconductivity of cell structure is done in terms of quantum efficiency (QE) as shown in figure 9 (d). The spectral response of the device is studied within the spectral range of 0.4 μm to 1.0 μm . Quantum efficiency is a measure of collection of charge carriers with respect to number of incident photons. As CdS buffer layer has higher band gap, it provides a wider window for absorption of photons, thus creating larger number of charge carriers and resulting in higher quantum efficiency in lower wavelength region, whereas in higher wavelength region QE of CdS becomes lower which ensures higher recombination in this structure. The higher values of quantum efficiencies are found for blue region of the light. Since blue light is absorbed closer to the junction, recombination effect is less effective for this wavelength region whereas at higher side of wavelength high recombination occurs, since the free carrier generated deeper in the bulk have to travel longer before being collected. This results higher recombination loss and in turn lower quantum efficiency in long wavelength region. Moreover, the absorption coefficient

decreases with the increasing of the photon wavelength, so the loss in absorption causes the spectral response to decrease quickly and thus the quantum efficiency.

3.5 Effect of buffer layer thickness

The effect of thickness of buffer layer on *J-V* characteristics for the two cell structures are shown in figures 9 (e)-9 (f). With the help of these characteristics J_{sc} , V_{oc} , η and *FF* are calculated at different thickness of buffer layers. The effect of thickness of buffer layer over performance parameters of these cell structures is shown in figures 10 (a)-10 (c). Figure 10 (a) and 10 (b) shows that as thickness of buffer layer increases, the current density as well as efficiency start to decrease for both the structures. This shows that at 50 nm the ratio of diffusion length to the thickness of the buffer layer is appropriate for collection of minority carriers. After this thickness all the photogenerated carriers are not able to reach the depletion region, which in turn decreases the current density and efficiency. The decrement in current density at lower thickness values is fast in ZnGeP₂/ZnSe structure, which shows that rate of recombination is higher in ZnGeP₂/ZnSe solar cell structure. Effect of thickness over fill factor for the two structures is shown in figure 10 (c). It is a measure of maximum power that can be achieved by a cell. As both the structures are showing the highest *FF* at 50nm thickness, ensures that at lower values of thickness charge collection is good because charge carriers are able to reach the electrodes. After this thickness charge collection suffers due to low values of diffusion length than the thickness of buffer layer. Further, with increment in thickness *FF* becomes almost constant because maximum effect of recombination over charge collection is achieved.

3.6 Effect of temperature

The effect of temperature over *J-V* characteristics for both the three structures is shown in Figure 10 (d) and 10 (e). Further, figures 10 (f)-11(e) show the effect of temperature over performance parameters for the two cell structures. In fig 10 (f), J_{sc} increases with temperature for both the structures considered. This effect can be understood in terms of band gap. The effect of temperature over energy band gap, E_g is given by Varshni equation [53]

$$E_g(T) = E_g(0) - \frac{\alpha T^2}{T + \beta} \quad (14)$$

Where $E_g(0)$ is the band gap energy at absolute zero on the Kelvin scale in the given material, and α and β are material-specific constants. This decrement in band gap is responsible for enhancement in current density values at higher temperature. Increase in temperature can be viewed as increase the energy of the charge carriers. Thus less energy is required to break the bond and conduction increases. As a consequence of the increase in temperature, there is a shift in quantum efficiency curves (figure 11 (a), 11 (b)). When the temperature of the cell is increased, thermal vibrations of the lattice becomes stronger, which causes reduction in lifetime and mobility of minority charge carriers. This in turn reduces the diffusion length and process of recombination becomes stronger. But with increase in temperature, the band gap is reduced, which enhances the production of charge carriers. In low and middle temperature range, there is equilibrium in between the phenomenon of charge generation and recombination. But with temperature, the absorption in wide band gap materials is improved for long wavelength region because of the phonons multiplication phenomenon [54]. So, the minority carriers production is increased with temperature in the range of long wavelengths, thus the photocurrent increases and consequently, the quantum efficiency. Further with temperature a sharp increment is found in V_{oc} (figure 11 (c)). The effect over V_{oc} can be understood as a measure of the amount of recombination in the device. As the temperature increases, the number of thermally generated carriers can exceed the number of dopant-generated carriers. Though the concentration of intrinsic carriers is very small; but it has very strong temperature dependence [55]. This increment in intrinsic carrier concentration causes the increase in reverse saturation current. The increment in reverse saturation current is responsible for decrement in open circuit voltage values. Also, the temperature dependence of v_{oc} is given by [56]

$$\frac{dV_{oc}}{dT} \approx \frac{dE_g/q}{dT} + \frac{V_{oc} - E_g/q}{T} \quad (15)$$

From eq. (15) it is inferred that the temperature dependence is mainly related to the term $\frac{V_{oc} - E_g/q}{T}$; which after integration provides a linear relationship $V_{oc} \propto -T$ as observed experimentally [56]. Therefore, the tendency of V_{oc} to decrease and J_{sc} to increase with increasing temperature in the solar cells are determining factor for efficiency with

variation in temperature. The overall effect of temperature has been studied for η as shown in figure 11 (d).

3.7 Effect of Band gap of absorption layer

The effect of band gap of absorption layer over performance parameters is studied. To find the effect of band gap, the results of ZnGeP₂ absorption layer with band gap 2.0 eV and 2.3 eV are compared. The effect of band gap of absorption layer over J-V characteristics of the cell are shown in figure 11 (f)-11 (g). These results show that the increment in band gap results in an increment in absorption of light, thus an increment in performance parameters is found (Table 6a and 6b). This improvement in parameters is due to the enhancement of absorption in longer wavelength region. This effect can be seen in quantum efficiency curves in figure 11 (f) and 11 (g). Hence, the study shows that ZnGeP₂ as absorption layer with CdS and ZnSe buffer can be promising solar cell model. ZnSe can be used as an option for CdS buffer layer, which is not only beneficial on the energy basis, but also helps in overcoming the serious environmental related problems due to the toxic nature of cadmium.

4 Conclusion

To conclude, results have been presented for the solid state properties such as structural, electronic, optical, elastic and thermal properties of the ZnGeP₂ semiconductor using the first-principles calculation. The structural properties in the chalcopyrite structure are obtained using the total energy as a function of volume; the derived equilibrium parameters are compared with experimental data. We compared electronic and optical properties calculated with the mBJ functional and spectroscopic ellipsometry data. We find that the mBJ functional provides an accurate description of the electronic and optical properties. The ZnGeP₂ has a direct band gap. We have also derived the static refractive index. Thermal properties such as Gruneisen parameter, volume expansion coefficient, bulk modulus, specific heat, entropy, debye temperature and hardness are calculated successfully at various temperatures and pressures, and trends are discussed. The ground state parameters of interest were obtained and showed good agreement with published experimental and theoretical data. An application of the material in solar cell device has been presented; here we have used AMPS-1D to investigate the dependence of the

buffer layer for thin layer ZnGeP₂ solar cells. A device modelling and detailed simulation study have been carried out over single junction ZnGeP₂ solar cell with a variety of buffer layers. The performance parameters of solar cells as open-circuit voltage (V_{oc}), the short-circuit current density (J_{sc}), the conversion efficiency η , Fill factor (FF) and quantum efficiency (QE) have been calculated. Also the effect of temperature and band gap of absorption

layer is studied and it is found that higher band gap of absorption layer improves the performance of solar cell. Thus the study shows that ZnSe can be considered as an alternative to CdS buffer layer and assumes greater significance under this scenario. To the best of our knowledge, most of the investigated parameters are reported for the first time and will further stimulate the research in the related field.

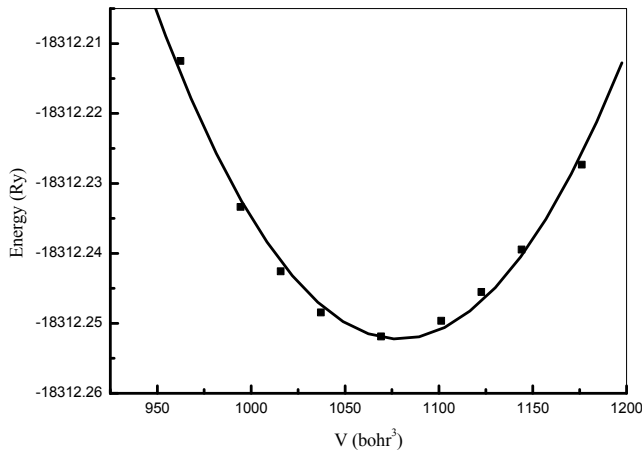


Figure 1. Calculated total energies as a function of volume

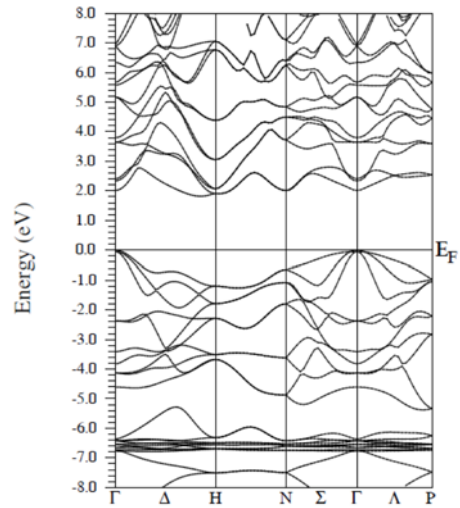
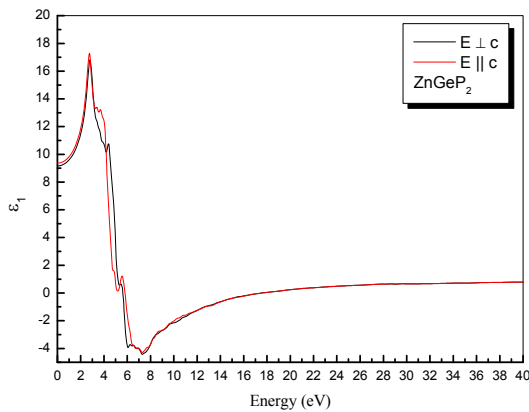
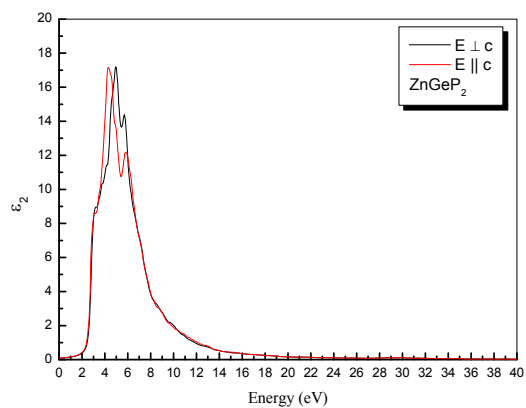


Figure 2. Band structures of ZnGeP₂



(a)



(b)

Figure 3. The calculated (a) real $\epsilon_1(\omega)$ and (b) imaginary $\epsilon_2(\omega)$ parts of complex dielectric constant for ZnGeP₂.

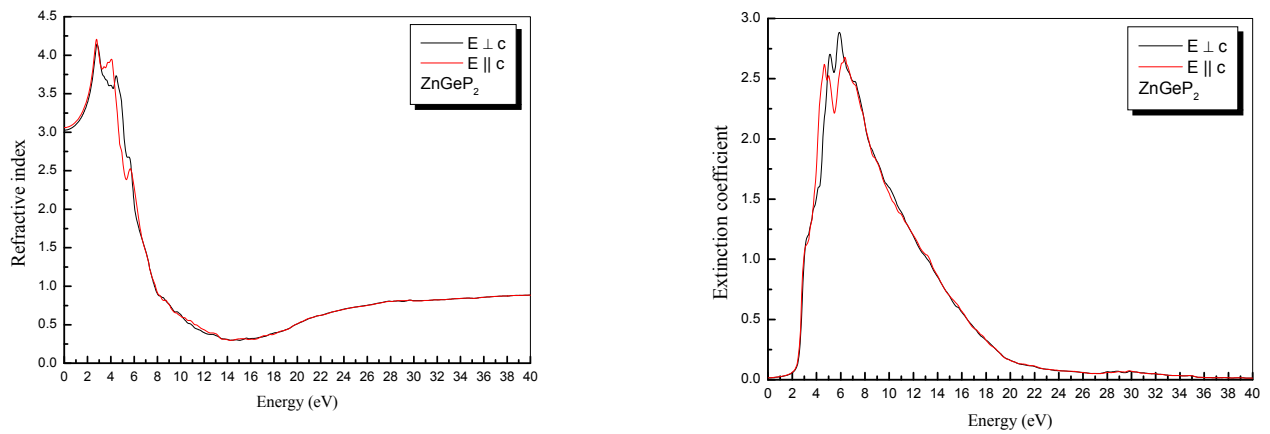
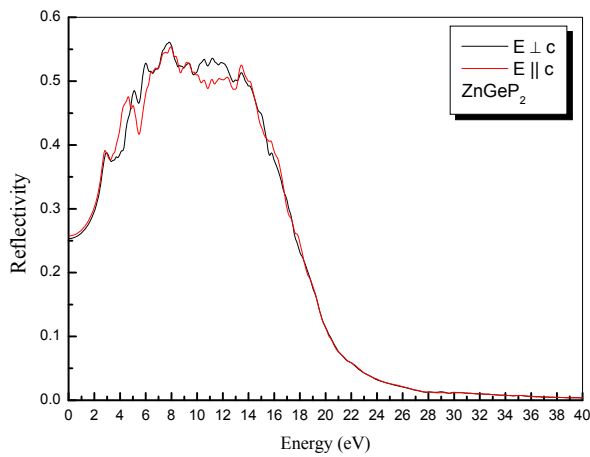
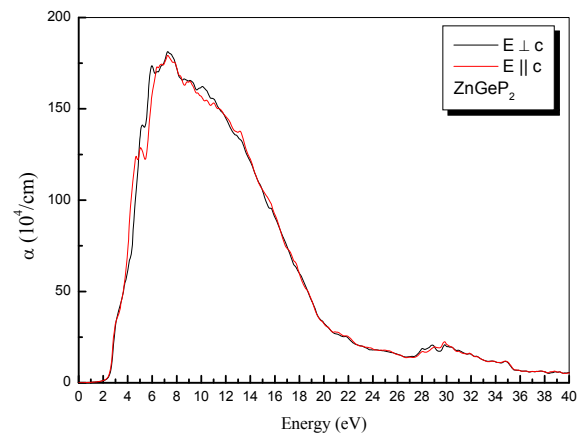


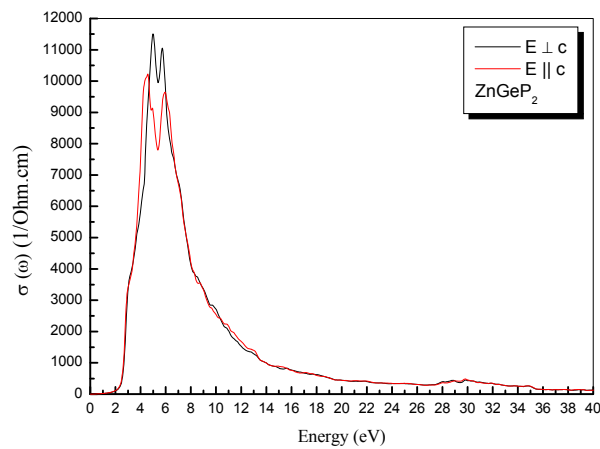
Figure 4. The calculated refractive index and extinction coefficient for ZnGeP₂.



(a)



(b)



(c)

Figure 5. (a) The calculated reflectivity ($R(\omega)$), (b) absorption coefficient ($\alpha(\omega)$) and (c) photoconductivity ($\sigma(\omega)$) for ZnGeP2.

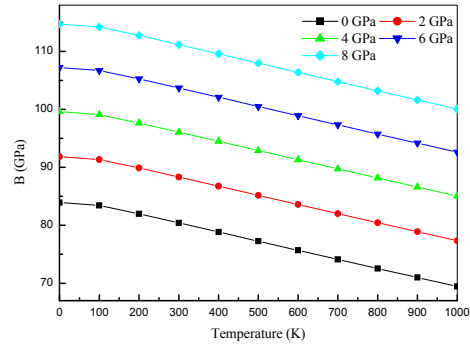
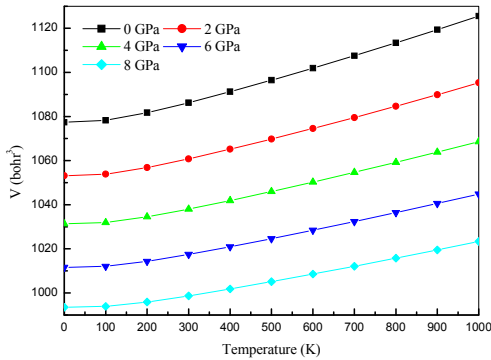


Figure 6. (a) Volume vs temperature at various pressures.

Figure 6. (b) Bulk modulus vs temperature at various pressures.

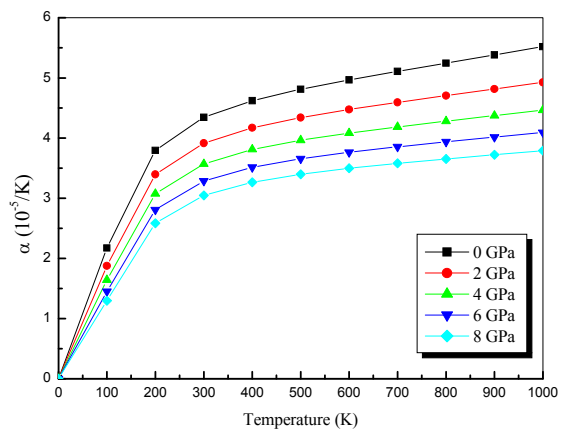
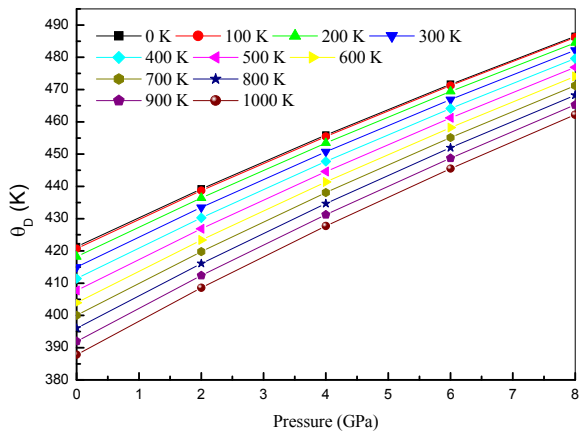


Figure 6. (d) Debye temperature vs pressure at various temperatures.

Figure 6. (e) Thermal expansion coefficients vs temperature at various pressures.

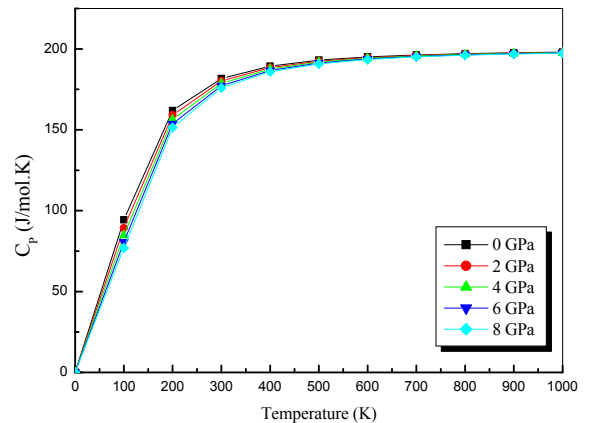
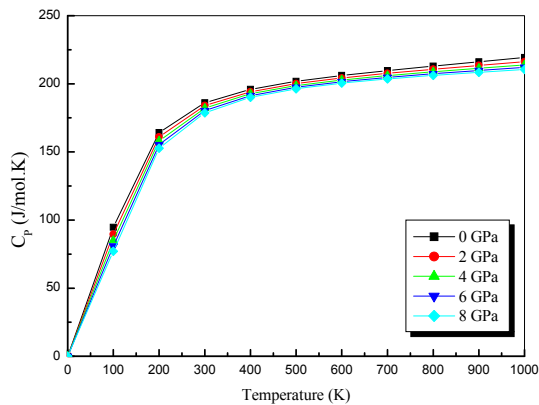


Figure 7. Heat capacity vs temperature at various pressures for ZnGeP₂.

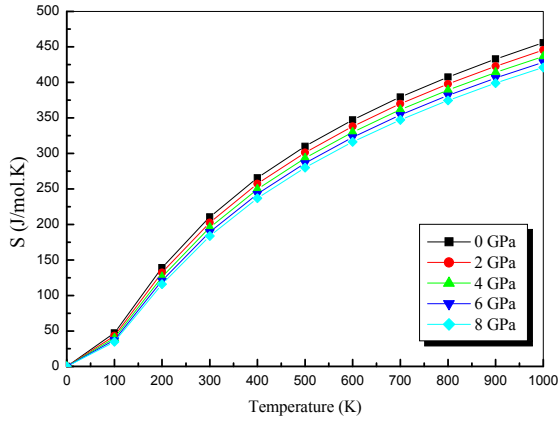


Figure 8. (a) Entropy vs temperature

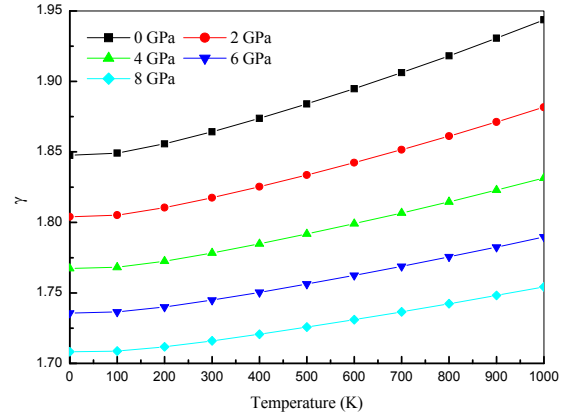


Figure 8. (b) Gruneisen parameter vs temperature

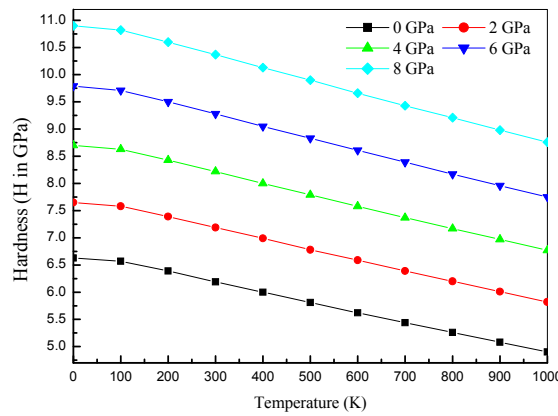


Figure 8. (c) Hardness vs temperature at various pressures

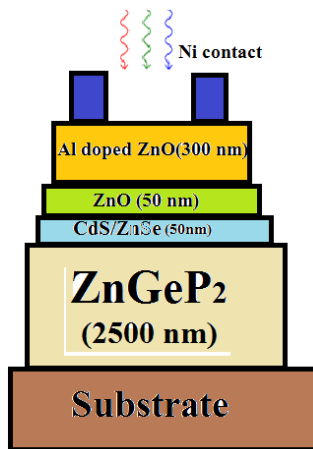


Figure 9 (a): The layer structure of ZnGeP₂ solar cell .

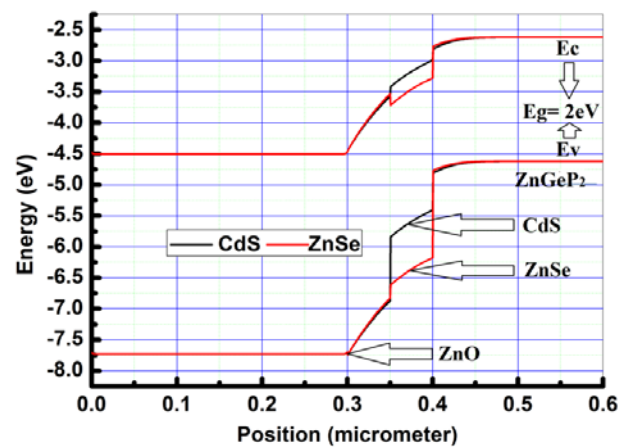


Figure 9 (b): The schematic energy-band diagram of a typical ZnGeP₂ /CdS or ZnSe solar cell under thermal

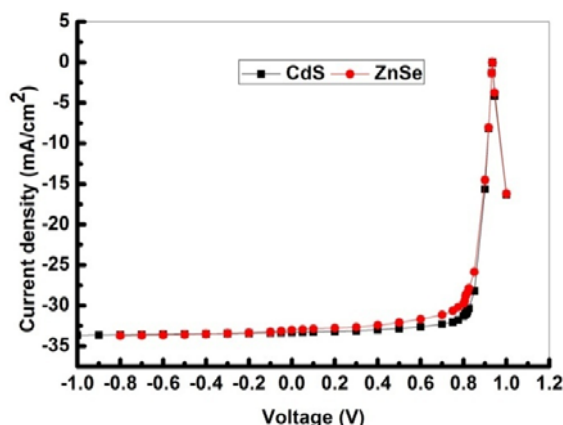


Figure 9 (c): Photo-current density-voltage (J-V) curves for the simulated results for 50nm thickness of CdS and ZnSe buffer layers.

equilibrium condition.

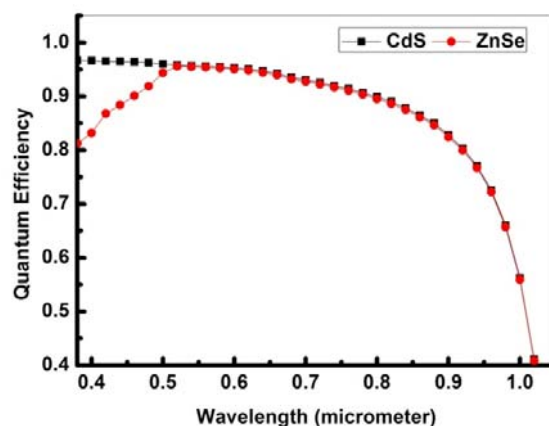


Figure 9 (d): Quantum efficiency curves for ZnGeP₂/CdS or ZnSe solar cell for 50 nm thickness of buffer layer.

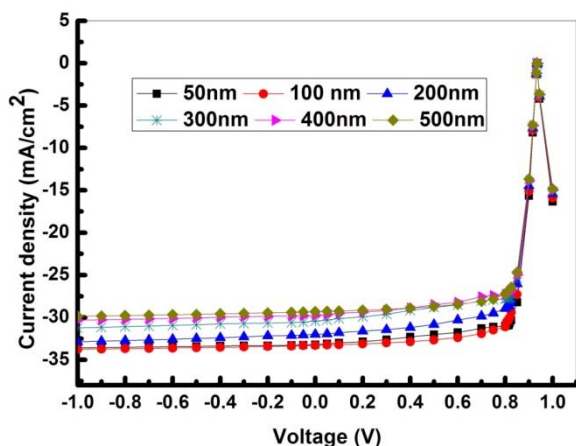


Figure 9 (e): Effect of thickness of buffer layer over J-V characteristics of ZnGeP₂/CdS solar cell.

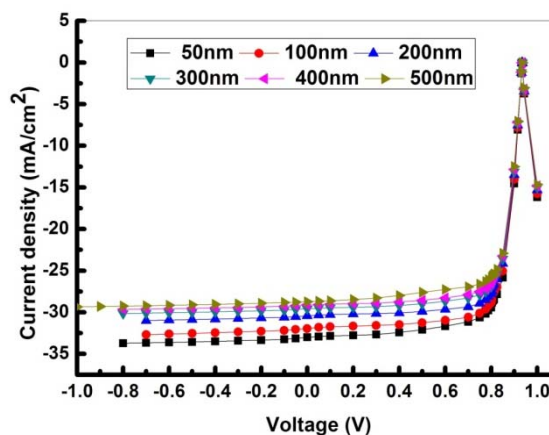


Figure 9 (f): Effect of thickness of buffer layer over J-V characteristics of ZnGeP₂/ZnSe solar cell.

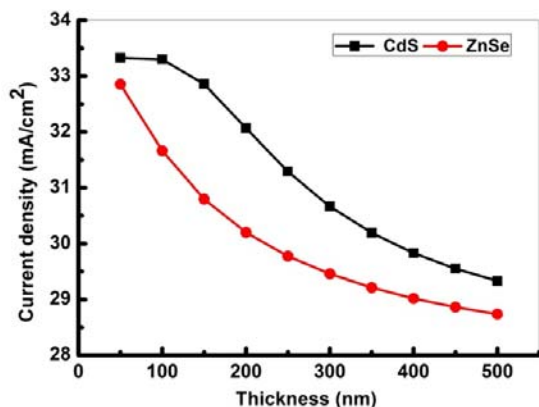


Figure 10 (a): Effect of thickness of buffer layer over current density of ZnGeP₂ solar cell with CdS/ZnSe buffer layer.

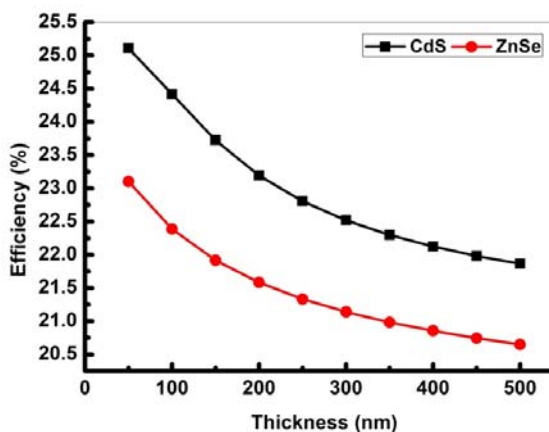


Figure 10 (b): Effect of thickness of buffer layer over efficiency of ZnGeP₂ solar cell with CdS/ZnSe buffer layer.

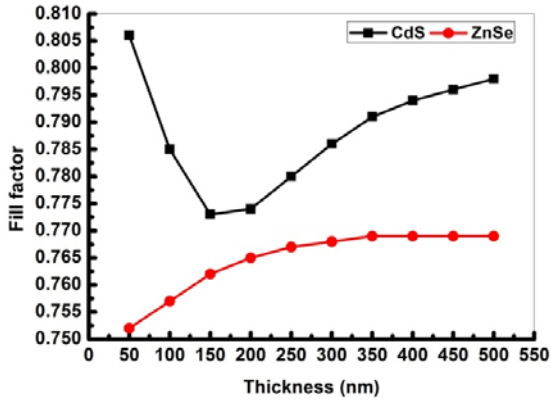


Figure 10 (c): Effect of thickness of buffer layer over fill factor of ZnGeP₂ solar cell with CdS/ZnSe buffer layer.

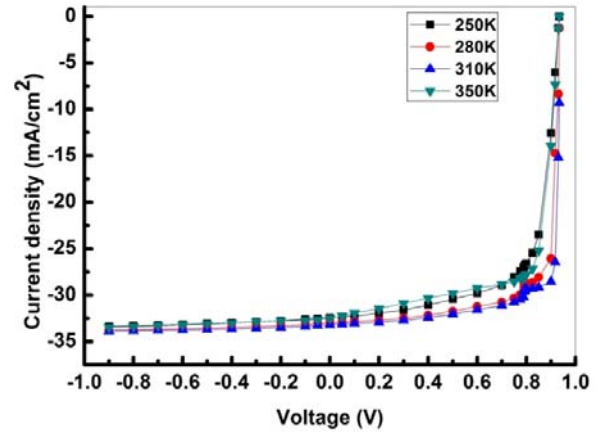


Figure 10 (d): Effect of temperature over J-V characteristics of ZnGeP₂/ZnSe solar cell.

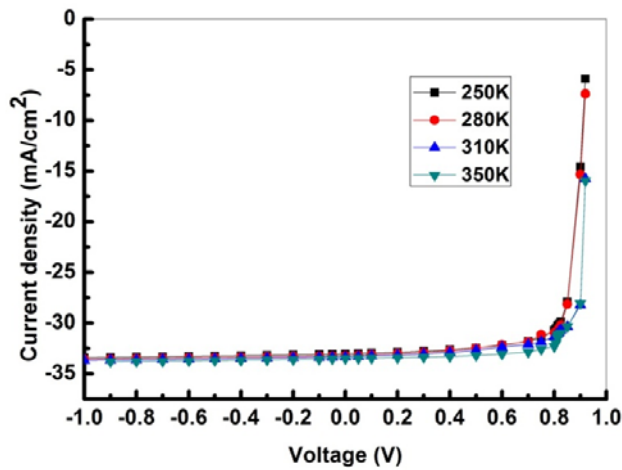


Figure 10 (e): Effect of temperature over J-V characteristics of ZnGeP₂/CdS solar cell.

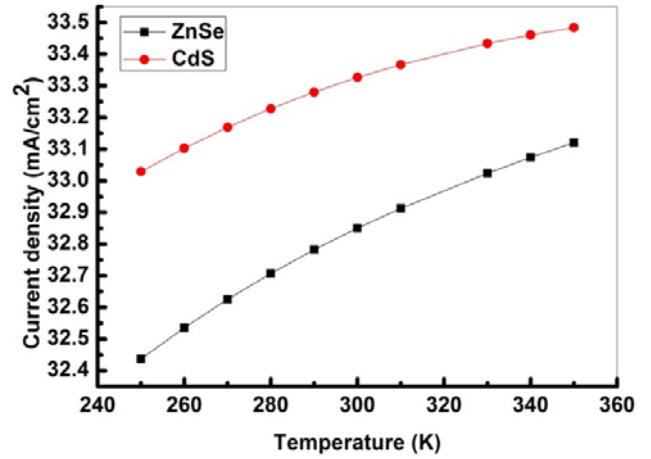


Figure 10 (f): Effect of temperature over current density of ZnGeP₂/CdS or ZnSe solar cell structures.

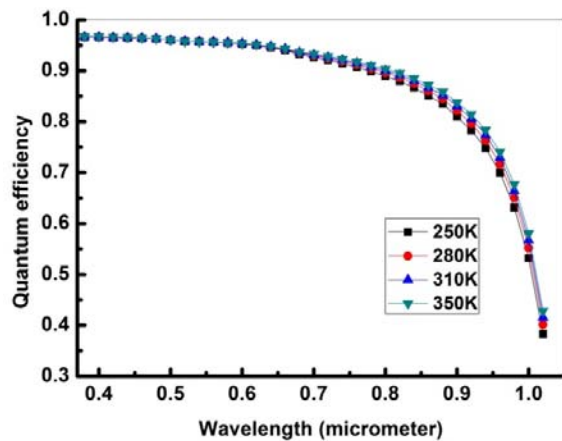


Figure 11 (a): Effect of temperature over quantum efficiency of ZnGeP₂/CdS solar cell

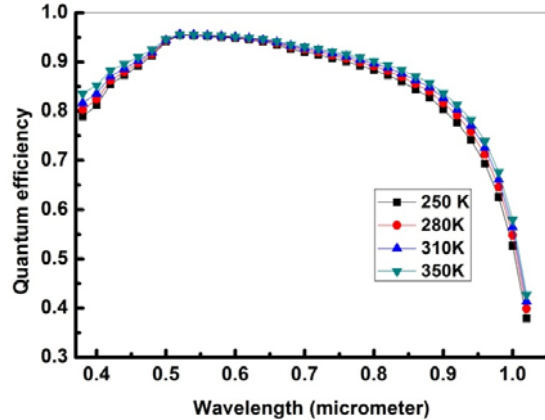


Figure 11 (b): Effect of temperature over quantum efficiency of ZnGeP₂/ZnSe solar cell.

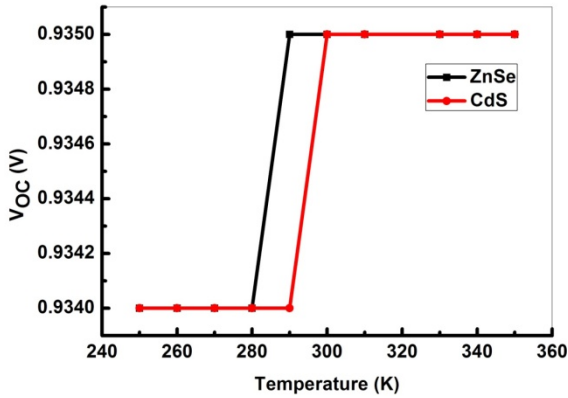


Figure 11 (c): Effect of temperature over open circuit voltage of ZnGeP₂/CdS or ZnSe solar cell structures

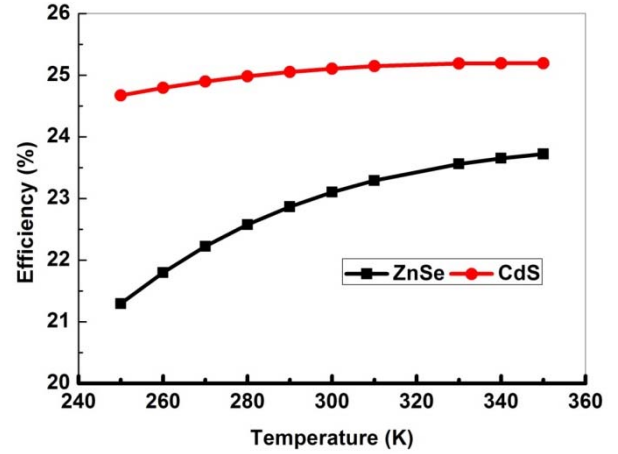


Figure 11 (d): Effect of temperature over efficiency of ZnGeP₂/CdS or ZnSe solar cell structures

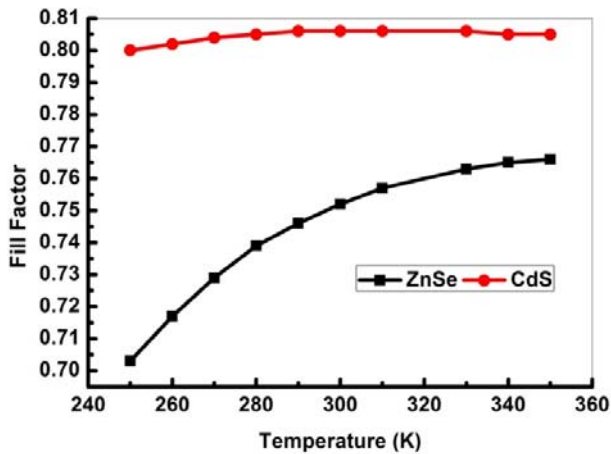


Figure 11 (e): Effect of temperature over fill factor of ZnGeP₂/CdS or ZnSe solar cell structures.

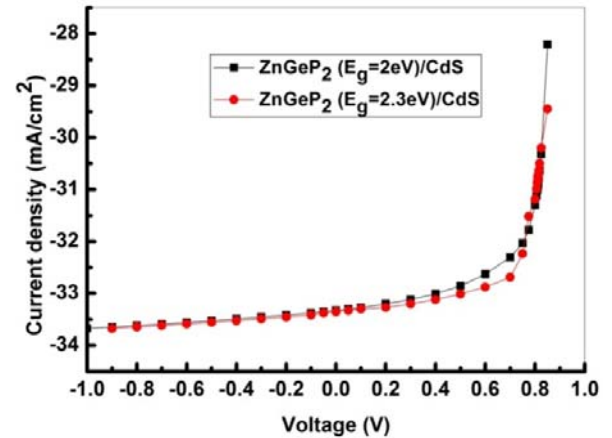


Figure 11 (f): Effect of band gap of absorption layer over J-V curves of ZnGeP₂/CdS solar cell.

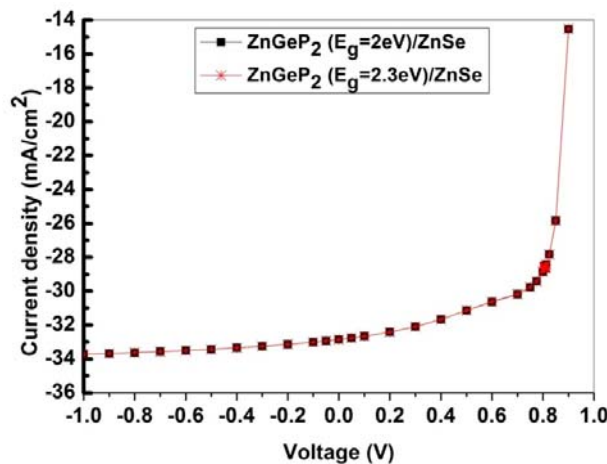


Figure 11 (g): Effect of band gap of absorption layer over J-V curves of ZnGeP₂/ZnSe solar cell.

Table 1. Structural equilibrium parameters, a, c, u, B and B' calculated in WC-GGA and thermal properties at 300 K; isothermal bulk modulus (B in GPa), Hardness (H in GPa), Gruneisen parameter (γ), Debye temperature (θ_D in K) and thermal expansion coefficient (α in $10^{-5}/K$) of ZnGeP₂.

Structural Analysis	a (Å)	c (Å)	u	B (GPa)	B'
	5.43, 5.46 ^{a,*}	10.73, 10.71 ^{a,*}	0.255	84	4.58
Thermal Analysis	B (GPa)	H (GPa)	γ	θ_D (K)	α ($10^{-5}/K$)
	80	6.19, 6.2 ^b	1.864	414, 410 ^c	4.345

^a Reference [45]; ^{*} Experimental; ^b Reference [50]; ^c Reference [51];

Table 2. The calculated minimum band gaps E_g (eV), refractive index (n) and dielectric constant for ZnGeP₂ compared with other experimental and theoretical data.

Crystals	E_g (eV)	this work	n this work	ϵ_∞ this work
ZnGeP ₂	2.0, 1.98 ^e	2.0-2.3 ^{d,*}	3.04, 3.10 ^{f,*}	9.26, 9.18 ^g

^d Reference [24]; ^e Reference [46]; ^f Reference [47]; ^g Reference [48]; ^{*} Experimental

Table 3. The lattice parameters of the deformed tetragonal unit cell, the expression relating the δ and ϵ variables, the finite Lagrangian strain tensor (Voigt notation) and the value of the second derivative, $(1/2V)(d^2E/d\epsilon^2)$, in terms of the elastic constants (ϵ being deformation coordinate and E the energy).

Strained cell	ϵ	Strain (η)	$dE^2/d\epsilon^2$
$(a + \delta, a + \delta, \frac{c + c\delta}{a}, 90, 90, 90)$	$\frac{(a + \delta)^2}{a^2} - 1$	$(\frac{\epsilon}{2}, \frac{\epsilon}{2}, \frac{c\epsilon}{2a}, 0, 0, 0)$	$\frac{1}{4}(C_{11} + C_{12}) + \frac{1}{8}C_{33} +$
$(a + \delta, a + \delta, c, 90, 90, 90)$	$\frac{(a + \delta)^2}{a^2} - 1$	$(\frac{\epsilon}{2}, \frac{\epsilon}{2}, 0, 0, 0, 0)$	$\frac{1}{4}(C_{11} + C_{12})$
$(a, a, \frac{c + c\delta}{a}, 90, 90, 90)$	$\frac{(c + \delta)^2}{c^2} - 1$	$(0, 0, \frac{\epsilon}{2}, 0, 0, 0)$	$\frac{1}{8}C_{33}$
$(a, a + \delta, c, 90, 90, 90)$	$\frac{(a + \delta)^2}{a^2} - 1$	$(0, \frac{\epsilon}{2}, 0, 0, 0, 0)$	$\frac{1}{8}C_{11}$
$(a, a, c, 90, 90 + \delta, 90)$	$\sin \delta$	$(0, 0, 0, 0, \epsilon, 0)$	C_{44}
$(a, a, c, 90, 90, 90 + \delta)$	$\sin \delta$	$(0, 0, 0, 0, 0, \epsilon)$	C_{66}

Table 4. Elastic constants C_{ij} (in GPa) of the ZnGeP₂ compared with available data.

C_{11}	C_{12}	C_{13}	C_{33}	C_{44}	C_{66}
133, 88 ^h	65, 55 ^h	66, 52 ^h	134, 82 ^h	64, 30 ^h	64, 27 ^h
B (GPa)	G (GPa)	Y (GPa)	ν	κ_a (GPa ⁻¹)	κ_c (GPa ⁻¹)
88	50	126	0.26	0.0038	0.0037

^h Reference [49];

Table 5: Material properties for the ZnGeP₂ solar cells simulation.

Layers	1-n+ZnO	2-n(i) ZnO	3-CdS	3-ZnSe	4-ZnGeP2
Parameters					
Thickness (nm)	300	50	50 ^a	50	2500
ϵ (dielectric constant)	9.26 ^b	9 ^c	9.4 ^b	10 ^c	9.26 ^d
μ_n (electron mobility in 10cm ² /Vs)	65.6 ^e	230 ^f	265 ^g	50 ^c	1000 ^h
μ_p (hole mobility in 10cm ² /Vs)	65 ⁱ	70 ^j	15 ^g	20 ^c	40 ^k
n/p (carrier density in cm ⁻³)	1.7×10 ^{19l}	5×10 ^{16l}	6×10 ^{16l}	1×10 ^{17m}	10 ^{12k}
E_g (eV) (optical band gap)	3.228 ⁿ	3.29 ⁿ	2.42 ^m	2.9 ^c	2 ^d
N_c (electron density in cm ⁻³)	1×10 ^{19l}	1×10 ^{19l}	1×10 ^{19l}	1.5×10 ^{18c}	6.8×10 ¹⁷
N_v (effective density in cm ⁻³)	1×10 ^{19l}	1×10 ^{19l}	1.6×10 ^{19l}	1.8×10 ^{19a}	1.5×10 ¹⁹
χ electron affinity (eV)	3.9 ^l	3.9 ^l	3.75 ^l	4.09 ^c	3.58 ^o

^a Reference [57]; ^b Reference [58]; ^c Reference [59]; ^d This work; ^e Reference [60]; ^f Reference [61]; ^g Reference[62]; ^hReference[63]; ⁱReference [64]; ^j Reference[65]; ^kReference[66]; ^lReference[67]; ^mReference[68]; ⁿReference[69]; ^oReference[70]

Table 6 (a): Simulated performance parameters of the solar cells for absorption layer ZnGeP₂ ($E_g = 2\text{eV}$)

Buffer layer	$\eta(\%)$	$V_{oc}(\text{mV})$	$J_{sc}(\text{mA}/\text{cm}^2)$	$FF(\%)$
ZnSe	21.139	0.934	29.456	0.768
CdS	22.518	0.934	30.666	0.786

Table 6 (b): Simulated performance parameters of the solar cells for absorption layer ZnGeP₂ ($E_g = 2.3\text{eV}$)

Buffer layer	$\eta(\%)$	$V_{oc}(\text{mV})$	$J_{sc}(\text{mA}/\text{cm}^2)$	$FF(\%)$
ZnSe	23.097	0.935	32.849	0.752
CdS	23.840	0.931	33.326	0.769

References:

- [1] Mukherjee, S., T. Maitra, A. Nayak, A. Pradhan, M. K. Mukhopadhyay, B. Satpati, and S. Bhunia. "Microstructural and light emission properties of ZnSnP₂ thin film absorber: Study of native defects" *Materials Chemistry and Physics* **204** (2018) 147-153.
- [2] Sharma, Sheetal, and Ajay Singh Verma. "Structural, electronic, optical, elastic and thermal properties of ZnXAs₂ (X= Si and Ge) chalcopyrite semiconductors" *The European Physical Journal B* **87** (2014) 159.
- [3] Sahin, S., Y. O. Ciftci, K. Colakoglu, and N. Korozlu. "First principles studies of elastic, electronic and optical properties of chalcopyrite semiconductor ZnSnP₂" *Journal of Alloys and Compounds* **529** (2012) 1-7.
- [4] Martinez, Aaron D., Emily L. Warren, Prashun Gorai, Kasper A. Borup, Darius Kuciauskas, Patricia C. Diplo, Brenden R. Ortiz et al. "Solar energy conversion properties and defect physics of ZnSiP₂" *Energy & Environmental Science* **9** (2016) 1031-1041.
- [5] Martinez, Aaron D., Angela N. Fioretti, Eric S. Toberer, and Adele C. Tamboli. "Synthesis, structure, and optoelectronic properties of II-IV-V₂ materials" *J. Materials Chemistry A* **5** (2017) 11418-11435.
- [6] Miyauchi, Keisuke, Takehiro Minemura, Keigo Nakatani, Hisayuki Nakanishi, Mutsumi Sugiyama, and Sho Shirakata. "Photoluminescence properties of ZnSnP₂ single crystals" *Physica Status Solidi C* **6** (2009) 1116-1119.
- [7] Nakatsuka, Shigeru, Shunsuke Akari, Jakapan Chantana, Takashi Minemoto, and Yoshitaro Nose. "Impact of Heterointerfaces in Solar Cells Using ZnSnP₂ Bulk Crystals" *ACS applied materials & interfaces* **9** (2017) 33827-33832.
- [8] Nakatsuka, Shigeru, Noriyuki Yuzawa, Jakapan Chantana, Takashi Minemoto, and Yoshitaro Nose "Solar cells using bulk crystals of rare metal-free compound semiconductor ZnSnP₂" *Physica Status Solidi A* **214** (2017) 1600650.
- [9] Scanlon, David O., and Aron Walsh. "Band gap engineering of ZnSnP₂ for high-efficiency solar cells" *Applied Physics Letters* **100** (2012) 251911.
- [10] Sreeparvathy, P. C., V. Kanchana, and G. Vaitheeswaran. "Thermoelectric properties of zinc based pnictide semiconductors" *J. Applied Physics* **119** (2016) 085701.
- [11] Verma, A. S. "Bulk modulus and hardness of chalcopyrite structured solids" *Materials Chemistry and Physics* **139** (2013) 256-261.
- [12] Yuzawa, Noriyuki, Jakapan Chantana, Shigeru Nakatsuka, Yoshitaro Nose, and Takashi Minemoto. "ZnSnP₂ thin-film solar cell prepared by phosphidation method under optimized Zn/Sn atomic ratio of its absorbing layer" *Current Applied Physics* **17** (2017) 557-564.
- [13] Zhang, Yujun. "Bandgap nature of chalcopyrite ZnXP₂ (X= Si, Ge, Sn)" *Computational Materials Science* **133** (2017): 152-158.
- [14] Madsen, Georg KH, Peter Blaha, Karlheinz Schwarz, Elisabeth Sjödtedt, and Lars Nordström. "Efficient linearization of the augmented plane-wave method" *Physical Review B* **64** (2001) 195134.
- [15] Schwarz, Karlheinz, Peter Blaha, and Georg KH Madsen. "Electronic structure calculations of solids using the WIEN2k package for material sciences" *Computer Physics Communications* **147** (2002) 71-76.
- [16] P. Blaha, K. Schwarz, G. K. H. Madsen, D. Kvasnicka, and J. Luitz, WIEN2k: An Augmented Plane Wave+Local Orbitals Program for Calculating Crystal Properties (Karlheinz Schwarz/Techn. Universität Wien, Austria, 2001).
- [17] Wu, Zhigang, and Ronald E. Cohen. "More accurate generalized gradient approximation for solids" *Physical Review B* **73** (2006) 235116.
- [18] Tran, Fabien, Robert Laskowski, Peter Blaha, and Karlheinz Schwarz. "Performance on molecules, surfaces, and solids of the Wu-Cohen GGA exchange-correlation energy functional" *Physical review B* **75** (2007) 115131.
- [19] Sham, Lu J., and Michael Schlüter. "Density-functional theory of the energy gap" *Physical Review Letters* **51** (1983) 1888.
- [20] Perdew, J. P., K. Burke, and M. Ernzerhof. "Perdew, burke, and ernzerhof reply" *Physical Review Letters* **80** (1998) 891.
- [21] Tran, Fabien, and Peter Blaha. "Accurate band gaps of semiconductors and insulators with a semilocal exchange-correlation potential" *Physical Review Letters* **102** (2009) 226401.

- [22] Blöchl, Peter E., Ove Jepsen, and Ole Krogh Andersen. "Improved tetrahedron method for Brillouin-zone integrations" *Physical Review B* **49** (1994) 16223.
- [23] Murnaghan, F. D. "The compressibility of media under extreme pressures" *Proceedings of the national academy of sciences of the United States of America* **30** (1944) 244.
- [24] Shaposhnikov, V. L., A. V. Krivosheeva, V. E. Borisenko, J-L. Lazzari, and F. Arnaud d'Avitaya. "Ab initio modeling of the structural, electronic, and optical properties of AIIBIVC2V semiconductors" *Physical Review B* **85** (2012) 205201.
- [25] Sun, Jian, Hui-Tian Wang, Nai-Ben Ming, Julong He, and Yongjun Tian. "Optical properties of heterodiamond B₂CN using first-principles calculations" *Applied Physics Letters* **84** (2004) 4544-4546.
- [26] Saha, Sonali, T. P. Sinha, and Abhijit Mookerjee. "Electronic structure, chemical bonding, and optical properties of paraelectric BaTiO₃" *Physical Review B* **62** (2000) 8828.
- [27] P. Y. Yu and M. Cardona, *Fundamentals of Semiconductors*, (Springer-Verlag, Berlin, 1996)
- [28] Cai, Meng-Qiu, Zhen Yin, and Ming-Sheng Zhang. "First-principles study of optical properties of barium titanate" *Applied Physics Letters* **83** (2003) 2805-2807.
- [29] Verma, A. S. "Correlation between ionic charge and the optical properties of zinc blende and complex crystal structured solids" *Physica Status Solidi (b)* **246** (2009) 192-199.
- [30] Rife, J. C., R. N. Dexter, P. M. Bridenbaugh, and B. W. Veal. "Optical properties of the chalcopyrite semiconductors ZnGeP₂, ZnGeAs₂, CuGaS₂, CuAlS₂, CuInSe₂, and AgInSe₂" *Physical Review B* **16** (1977) 4491.
- [31] J. F. Nye, *Physical Properties of Crystals, Their Representation by Tensors and Matrices*, Oxford Univ. Press, Oxford, USA, 1985
- [32] W. Voigt, *Lehrbuch der Kristallphysik*, Teubner, Leipzig, 1928
- [33] Shein, I. R., and A. L. Ivanovskii. "Elastic properties of quaternary oxypnictides LaOFeAs and LaOFeP as basic phases for new 26–52 K superconducting materials from first principles." *Scripta Materialia* **59** (2008) 1099-1102.
- [34] Reuss, A. "Mittelung von Fließgrenze und elastischen Eigenschaften" *Z. angew. Math. Mech. Bd* **9** (1929) 49.
- [35] Hill, Richard. "The elastic behaviour of a crystalline aggregate" *Proceedings of the Physical Society. Section A* **65** (1952) 349.
- [36] Pugh, S. F. "XCII. Relations between the elastic moduli and the plastic properties of polycrystalline pure metals" *The London, Edinburgh, and Dublin Philosophical Magazine and Journal of Science* **45** (1954): 823-843.
- [37] Chen, Kuiying, L. R. Zhao, and John S. Tse. "Ab initio study of elastic properties of Ir and Ir₃X compounds" *J Applied Physics* **93** (2003) 2414-2417.
- [38] Chen, K., L. R. Zhao, J. S. Tse, and J. R. Rodgers. "Elastic properties of platinum Rh and Rh₃X compounds" *Physics Letters A* **331** (2004) 400-403.
- [39] Blanco, M. A., E. Francisco, and V. Luana. "GIBBS: isothermal-isobaric thermodynamics of solids from energy curves using a quasi-harmonic Debye model" *Computer Physics Communications* **158** (2004) 57-72.
- [40] Blanco, M. A., A. Martín Pendás, E. Francisco, J. M. Recio, and R. Franco. "Thermodynamical properties of solids from microscopic theory: applications to MgF₂ and Al₂O₃" *J. Molecular Structure: THEOCHEM* **368** (1996) 245-255.
- [41] Flórez, M., J. M. Recio, E. Francisco, M. A. Blanco, and A. Martín Pendás. "First-principles study of the rocksalt–cesium chloride relative phase stability in alkali halides" *Physical Review B* **66** (2002) 144112.
- [42] Francisco, E., M. A. Blanco, and G. Sanjurjo. "Atomistic simulation of Sr F 2 polymorphs" *Physical Review B* **63** (2001) 094107.
- [43] J. P. Poirier, *Introduction to the Physics of Earth's Interior*, Cambridge University Press, Oxford, 2000, p. 39
- [44] Verma, A. S., and S. R. Bhardwaj. "Correlation between ionic charge and the mechanical properties of complex structured solids" *J. Physics: Condensed Matter* **19** (2006) 026213.
- [45] Kimmel, G., Y. Shimony, O. Raz, and M. P. Dariel. "Order and Disorder in ZnGeP₂ Crystals" *Materials Structure* **6** (1999) 149.
- [46] Verma, Ajay Singh, Sheetal Sharma, and V. K. Jindal. "Evaluating optical parameters from electronic structure and crystal structure for binary (anb 8-n) and ternary tetrahedral semiconductors" *Modern Physics Letters B* **24** (2010) 2511-2524.

- [47] Verma, A. S. "Correlation between ionic charge and the optical properties of zinc blende and complex crystal structured solids" *Physica Status Solidi B* **246** (2009) 192-199.
- [48] Verma, A. S., and D. Sharma. "Dielectric constants of AIBIIC2VI and AIIBIVC2V chalcopyrite semiconductors" *Physica Scripta* **76** (2007) 22.
- [49] Verma, A. S., Sheetal Sharma, R. Bhandari, B. K. Sarkar, and V. K. Jindal. "Elastic properties of chalcopyrite structured solids" *Materials Chemistry and Physics* **132** (2012) 416-420.
- [50] Verma, A. S. "Bulk modulus and hardness of chalcopyrite structured solids" *Materials Chemistry and Physics* **139** (2013) 256-261.
- [51] Kumar, V., A. K. Shrivastava, Rajib Banerji, and D. Dhirhe. "Debye temperature and melting point of ternary chalcopyrite semiconductors" *Solid State Communications* **149** (2009) 1008-1011.
- [52] B. G. Streetman, S. K. Banerjee, *Solid State Electronic Devices* 6th ed. Pearson int. ed., (2010)
- [53] Varshni, Yatendra Pal. "Temperature dependence of the energy gap in semiconductors" *Physica* **34** (1967) 149-154.
- [54] B. O. Seraphin, *Solar Energy Conversion—Solid State Physics Aspects Topics in Applied Physics, Volume 31*, Springer, (1979)
- [55] S. M. Sze, *Physics of semiconductor devices*, 2nd ed. John Wiley and Sons, NY (1981).
- [56] P. Würfel, *Physics of Solar Cells*, Wiley-VCH Verlag, Weinheim, 2005
- [57] M. A. Green, *Solar Cells, Operating Principles, Technology and System Applications*, Prentice Hall Inc., (1982)
- [58] Young, K. F., and H. P. R. Frederikse. "Compilation of the static dielectric constant of inorganic solids" *Journal of Physical and Chemical Reference Data* **2** (1973): 313-410.
- [59] Olopade, M. A., O. O. Oyebola, and B. S. Adeleke. "Investigation of some materials as buffer layer in copper zinc tin sulphide (Cu₂ZnSnS₄) solar cells by SCAPS-1D" *Advances in Applied Science Research* **3** (2012) 3396-3400.
- [60] Kim, Kyoung-Kook, Shigeru Niki, Jin-Yong Oh, June-O. Song, Tae-Yeon Seong, Seong-Ju Park, Shizuo Fujita, and Sang-Woo Kim. "High electron concentration and mobility in Al-doped n-ZnO epilayer achieved via dopant activation using rapid-thermal annealing" *J. Appl. Phys.* **97** (2005) 066103.
- [61] Yang, Xiaocheng, Chunchuan Xu, and N. C. Giles. "Intrinsic electron mobilities in CdSe, CdS, ZnO, and ZnS and their use in analysis of temperature-dependent Hall measurements" *J. Applied Physics* **104** (2008) 073727.
- [62] Spear, W. E., and J. Mort. "Electron and hole transport in CdS crystals" *Proceedings of the Physical Society* **81** (1963) 130.
- [63] Ray, B., A. J. Payne, and G. J. Burrell. "Preparation and some physical properties of ZnGeP₂" *Physica Status Solidi B* **35** (1969) 197-204.
- [64] Bodea, M. A., G. Sbarcea, Gururaj V. Naik, Alexandra Boltasseva, T. A. Klar, and J. D. Pedarnig. "Negative permittivity of ZnO thin films prepared from aluminum and gallium doped ceramics via pulsed-laser deposition" *Applied Physics A* **110** (2013) 929-934.
- [65] B. K. Meyer, ZnO: electron and hole mobilities, *Landolt-Börnstein-Group III Condensed Matter*, **44D** (2011) 610.
- [66] Dietz, N., I. Tsveybak, W. Ruderman, G. Wood, and K. J. Bachmann. "Native defect related optical properties of ZnGeP₂" *Applied physics letters* **65** (1994) 2759-2761.
- [67] Ray, J. R., C. J. Panchal, M. S. Desai, and U. B. Trivedi. "Simulation of CIGS thin film solar cells using AMPS-1D." (2011).
- [68] Burgelman, Marc, Koen Decock, Samira Khelifi, and Aimi Abass. "Advanced electrical simulation of thin film solar cells" *Thin Solid Films* **535** (2013) 296-301.
- [69] Mondal, S. B. S. R., S. R. Bhattacharyya, and P. Mitra. "Effect of Al doping on microstructure and optical band gap of ZnO thin film synthesized by successive ion layer adsorption and reaction" *Pramana J Physics* **80** (2013) 315-326.
- [70] C. M. Wolfe, N. Holonyak, G. E. Stillman, *Physical Properties of Semiconductors*, Prentice Hall, USA (1989).